

# Dynamic Contrast-Enhanced MRI in the Study of Brain Tumors. Comparison Between the Extended Tofts-Kety Model and a Phenomenological Universalities (PUN) Algorithm

Maurizio Bergamino<sup>1,2</sup> · Laura Barletta<sup>3</sup> · Lucio Castellan<sup>3</sup> · Gianluigi Mancardi<sup>1,2</sup> · Luca Roccatagliata<sup>2,3,4</sup>

Published online: 17 March 2015  
© Society for Imaging Informatics in Medicine 2015

**Abstract** Dynamic contrast-enhanced magnetic resonance imaging (DCE-MRI) is a well-established technique for studying blood–brain barrier (BBB) permeability that allows measurements to be made for a wide range of brain pathologies, including multiple sclerosis and brain tumors (BT). This latter application is particularly interesting, because high-grade gliomas are characterized by increased microvascular permeability and a loss of BBB function due to the structural abnormalities of the endothelial layer. In this study, we compared the extended Tofts-Kety (ETK) model and an extended derivate class from phenomenological universalities called EU1 in 30 adult patients with different BT grades. A total of 75 regions of interest were manually drawn on the MRI and subsequently analyzed using the ETK and EU1 algorithms. Significant linear correlations were found among the parameters obtained by these two algorithms. The means of  $R^2$  obtained using ETK and EU1 models for high-grade tumors were 0.81 and 0.91, while those for low-grade tumors were 0.82 and 0.85, respectively; therefore, these two models are equivalent. In conclusion, we can confirm that the application

of the EU1 model to the DCE-MRI experimental data might be a useful alternative to pharmacokinetic models in the study of BT, because the analytic results can be generated more quickly and easily than with the ETK model.

**Keywords** DCE-MRI · Brain tumors · Blood–brain barrier · Extended Tofts-Kety model · EU1 algorithm

## Introduction

Many pathologies relating to the central nervous system affect the integrity of the blood–brain barrier (BBB). For instance, inflammatory diseases, such as multiple sclerosis [1, 2], chronic and acute cerebrovascular pathology [3, 4], and brain tumors, induce BBB damage.

The BBB in patients with brain tumors is structurally and functionally abnormal [5]; the tumor blood vessels are tortuous, disorganized, and highly permeable because of abnormalities in their endothelial walls [6]. For instance, glioblastoma multiforme (GBM), which is one of the most common and most aggressive vascular primary brain tumors in adults, is characterized by increased microvascular permeability and a loss of BBB function due to structural abnormalities of the endothelial layer. In particular, these abnormalities exist as open endothelial gaps (interendothelial junctions and transendothelial channels), cytoplasmic vesicles (caveolae and vesicular vacuolar organelles), and fenestrations [7].

Dynamic contrast-enhanced magnetic resonance imaging (DCE-MRI) is a well-established technique for studying BBB permeability, and it is useful to study and monitor treatment of the BBB's integrity in patients with brain tumors. This technique involves the serial acquisition of T1-weighted images before, during, and after the injection of a paramagnetic contrast agent (CA) [8]. In DCE-MRI, kinetic parameters,

---

✉ Maurizio Bergamino  
maurizio.bergamino@gmail.com

- <sup>1</sup> Department of Neuroscience, Rehabilitation, Ophthalmology, Genetics, Maternal and Child Health, University of Genoa, Via De Toni 5, 16132 Genoa, Italy
- <sup>2</sup> Magnetic Resonance Research Centre on Nervous System Diseases, University of Genoa, Via De Toni 5, 16132 Genoa, Italy
- <sup>3</sup> Department of Diagnostic and Interventional Neuroradiology, San Martino University Hospital, Largo Rosanna Benzi 10, 16132 Genoa, Italy
- <sup>4</sup> Department of Health Sciences, University of Genoa, Largo Rosanna Benzi 10, 16132 Genoa, Italy

such as the volume transfer constant between blood plasma and extravascular extracellular space (EES) ( $K^{\text{trans}}$ ), the volume of EES per unit volume of tissue ( $v_e$ ), the blood plasma volume per unit volume of tissue ( $v_p$ ), and the rate constant between EES and the blood plasma ( $k_{ep}$ ) can be assessed [9].

The standard Tofts-Kety (TK) model [9] and the extended Tofts-Kety (ETK) model [10] are the theoretical models that have been used the most in the past to study DCE-MRI data. The ETK model is generally recommended for tumor characterization; it makes it possible to obtain the essential permeability parameters that correlate with immunohistochemical markers of tumor angiogenesis, microvessel density, and tumor grade [11]. With the ETK model, it is possible to assess  $K^{\text{trans}}$ ,  $v_e$ , and  $v_p$ , while with the TK model, it is only possible to evaluate  $K^{\text{trans}}$  and  $v_e$ ; therefore, it can be used only in tissues that are weakly vascularized. It is possible to use other more complicated theoretical models for the DCE-MRI data, such as the adiabatic approximation to the tissue homogeneity model, the distributed capillary adiabatic tissue homogeneity model, and the two-compartment exchange model. Different problems in the evaluation of kinetic parameters can occur due to these different models. Hence, it is very important to pay attention to the algorithm used for the DCE-MRI data fitting [12–14].

The DCE-MRI signal provides a relationship between the measured signal time course  $S(t)$  and the concentration  $C(t)$  of CA. However, the DCE-MRI signal cannot be used directly for kinetic model fitting, because it does not proportionally reflect the CA concentration in tissues. For this reason, the implementation of the pharmacokinetic model typically requires the knowledge of T1 pre-contrast values in the whole brain and the arterial input function (AIF) estimation.

As an alternative to the models described above, empirical functions can be used to fit DCE-MRI curves accurately, without making assumptions about tumor physiology. Fan et al. [15] used an empirical mathematical model for DCE-MRI in order to differentiate between benign and malignant breast tumors. Conversely, Gliozzi et al. [16] and Mazzetti et al. [17] demonstrated that an empirical approach based on phenomenological universalities (PUN) is able to fit DCE-MRI experimental data on the spine and prostate tumors, respectively. The PUN algorithm was used for the first time by Castorina et al. [18] and Delsanto [19], and subsequently used in a wide range of applications [20, 21].

In this study, we compared the ETK model and a derivate class of PUN, called EU1 [16], applied to DCE-MRI data on patients with different astrocytic tumors. We presented the assessments and statistical correlations of different parameters calculated by these two methods. We also evaluated the quality of the results' fit by using standard  $R^2$  criteria. The EU1 algorithm works on the MR signal intensity and not on the CA concentration. Provided that it does not need both the T1 pre-contrast values in the brain and the estimation of AIF, its data

are easier and faster to analyze than those obtained when using the ETK model from a computing perspective.

## Materials and Methods

### Patients

We studied retrospectively 30 adult patients (16 females and 14 males; mean age±standard deviation=58.8±8.1 years; age range=43–75 years) with different astrocytic tumors. The World Health Organization's (WHO) [22] classification was used to determine the histological grades of each lesion. For all patients recruited in this study, the diagnoses were confirmed by histopathology. In addition, patients were included only if they were not receiving radiation, chemotherapy, or a combination of both.

The tumors consisted of 20 glioblastomas multiforme (GBM) (for a total of 56 ROIs) (WHO grade IV), three anaplastic astrocytomas (for a total of six ROIs) (WHO grade III), and seven low-grade gliomas (for a total of 13 ROIs) (WHO grade II).

A total of 75 regions of interest (ROIs) in the tumor regions were manually drawn on the DCE-MRI by a radiologist. ROIs were drawn using ImageJ software [<http://imagej.nih.gov/ij/>]. The tumor extension was evaluated mainly on the T1 contrast-enhanced images (CE-T1) and on the T2 fluid attenuated inversion recovery (FLAIR) for low-grade tumors. The CE-T1 and FLAIR images were coregistered to DCE-MRI by using FLIRT, included in the FMRIB Software Library (FSL version 5.0.4) [23]. Multiple ROIs were drawn in order to avoid areas of necrosis and large blood vessels and when the tumor extended onto more slices. We did not include satellite lesions.

This study was approved by our local IRB. The protocol associated with this study meets all criteria from our IRB regarding retrospective studies. Informed consent was obtained from each participating patient, and it included information to the patient that an additional sequence with longer scanning time and contrast agent would be utilized.

### Imaging Protocol

MRI was performed using a 1.5-T clinical system (Siemens Magnetom Avanto, Erlangen, Germany) with receive eight-channel head coil. The following image sequences were acquired: T2-weighted (TR/TE=3800/95 ms; acquisition matrix=320×384; NEX=2; field of view=250×300 mm; slice thickness=5 mm, flip angle=150°), FLAIR (TR/TE=9000/119 ms; acquisition matrix=320×384; NEX=1; field of view=250×300 mm; slice thickness=5 mm); and T1-weighted (TR/TE=500/10 ms; acquisition matrix=320×384; NEX=1; field of view=250×300 mm; slice thickness=5 mm, flip angle=80°). In order to calculate the T1 pre-

contrast values in the brain, fast low-angle shot (FLASH) axial 3D T1-weighted images (TR/TE=6.7/1.0 ms; acquisition matrix=320×384; NEX=1; field of view=250×300 mm; slice thickness=5 mm) were acquired with multiple flip angles (5, 10, 15, 20, and 30°) before the intravenous injection of CA.

The DCE-MRI sequence was started immediately after the intravenous administration of a gadolinium-based CA (gadobutrol 0.1 ml/kg) by a power injector (Spectris Solaris EP Medrad) at a rate of 5 mL/s. Dynamic axial 3D T1-weighted Turbo FLASH images (TR/TE=6.7/1.0 ms; acquisition matrix=320×384; NEX=1; field of view=250×300 mm; slice thickness=5 mm; flip angle=30°; number of slices=20) were acquired for 30 time points (234 s). For the data analysis, we removed the first and the last slices in every patient.

### Imaging Post-Processing

The ETK model can be described by an impulse response formalism [24]:

$$C_t(t) = (v_p(t) + K^{\text{trans}} \cdot \exp[-k_{\text{ep}}t]) \otimes C_a(t) \quad (1)$$

where  $C_t(t)$  is the total tissue contrast concentration, and  $C_a(t)$  is the contrast concentration in the arterial whole blood. The rate constant between EES and the blood plasma ( $k_{\text{ep}}$ ) is equal to  $K^{\text{trans}}/v_e$ , and the  $\otimes$  symbol represents the convolution. In calculating the convolution,  $C_t(t)$  becomes:

$$C_t(t) = v_p C_p(t) + K^{\text{trans}} \int C_p(\tau) \exp[-k_{\text{ep}}(t-\tau)] d\tau \quad (2)$$

where  $C_p(t)$  is the tracer concentration in the blood plasma ( $C_p(t) = C_a(t)/(1-\text{Hct})$ ). Hct is the hematocrit. We used an Hct value of 0.45, because it is the mean value in large vessels for adult human populations [14].

In order to obtain the tissue contrast concentration, we calculated pixel-wise T1 pre-contrast maps by the least-square fitting of the theoretical equation:

$$S(t) = \frac{M_0 \left( 1 - \exp\left[-\frac{\text{TR}}{T_1}\right] \right) \sin \alpha}{1 - \cos \alpha \cdot \exp\left[-\frac{\text{TR}}{T_1}\right]}; \text{TR} \gg T_2^* \quad (3)$$

where  $S(t)$  is the MRI signal, TR is the repetition time,  $\alpha$  is the flip angle, and  $M_0$  is a factor proportional to the equilibrium magnetization. T1 pre-contrast maps were generated by fitting the pixel-wise image intensities of Eq. (3) at the flip angles of

5, 10, 15, 20, and 30°. Subsequently, the  $T_1$  and  $S_0$  values were used to estimate the voxel  $R_1$  time courses, or relaxation rates, from the acquired signal intensity time courses by Eq. (4):

$$R_1(t) = -\frac{1}{\text{TR}} \ln \left[ \frac{1 - \left( \frac{S(t)-S(0)}{S_0 \sin \alpha} + \frac{1-m}{1-(m \cdot \cos \alpha)} \right)}{1 - \cos \alpha \left( \frac{S(t)-S(0)}{S_0 \sin \alpha} + \frac{1-m}{1-(m \cdot \cos \alpha)} \right)} \right] \quad (4)$$

where  $\alpha$  is the flip angle of the DCE-MRI sequence ( $\alpha=30^\circ$ ),  $m = \exp[-\text{TR}/T_1]$ ,  $S(0)$  and  $S(t)$  are the signal intensities at time  $t=0$ , and time  $t$ , respectively. Then we calculated the  $C(t)$  by using:

$$R_1(t) = R_{10} + r_1 C(t) \quad (5)$$

where  $R_{10}$  is the relaxation rate before the tracer injection and  $r_1$  is the relaxivity of the CA ( $r_1=4.3 \text{ mM}^{-1} \text{ s}^{-1}$ ) [25]. Therefore, fitting  $C(t)$  with Eq. (2),  $K^{\text{trans}}$ ,  $v_e$ ,  $v_p$ , and subsequently  $k_{\text{ep}}$  can be obtained.

PUN formalism is an empirical tool which represents the experimental data of any given dataset analytically, independent of the application field. In the past few years, the PUN theory has been applied to several studies of DCE-MRI data [16, 26].

$$S(t) = \exp \left[ rt + \frac{1}{\beta} (a_0 - r) (\exp(\beta t) - 1) \right] \quad (6)$$

With EU1 class (Eq. 6), it is possible to obtain the following three kinetic parameters:  $a_0$ , which controls the steepness of the DCE-MRI curve at  $t=0$ , and therefore, during the wash-in phase (the first part of the DCE-MRI curve);  $\beta$ , which is the inverse proportion to the time the system takes to reach the knee of the curve. The sign of  $r$  determines the behavior of the second part of the curve, and its absolute value is linked to the rapidity of the change. For  $r>0$ , one can observe a further enhancement of the intensity of the signal, while for  $r<0$ , there is a wash-out phase [16].

### Arterial Input Functions and T1 Maps

Arterial input functions (AIFs) were assessed by fitting the CA concentration on the superior sagittal sinus by using a bi-exponential function for every patient, and T1 maps on the whole brains were calculated using a variable flip angle method with five different flip angles (see *Imaging protocol*).

### Results

DCE-MRI curves were analyzed using the ETK model (Eq. 2) and the EU1 algorithm (Eq. 6). Moreover, in order to evaluate the quality of the fit of the results, standard  $R^2$  criteria were used. We calculated the means and standard deviations of the permeability parameters inside different ROIs. All results are expressed as mean±standard deviation.

We found a mean value of  $K^{trans}$  in grade IV tumors of  $0.22\pm0.11 \text{ min}^{-1}$ , a mean value of  $K^{trans}$  in grade III tumors of  $0.18\pm0.07 \text{ min}^{-1}$ , and a mean value of  $K^{trans}$  in low-grade tumors of  $0.033\pm0.018 \text{ min}^{-1}$ .

The mean values for  $a_0$  were  $53.6\pm18.9$ ,  $38.4\pm17.3$ , and  $22.3\pm11.0 \text{ min}^{-1}$  for grade IV, grade III, and low-grade tumors, respectively. A significant Pearson correlation was found between  $K^{trans}$  and  $a_0$  in a total of 75 ROIs ( $r=0.71$ ,  $p<0.0001$ ; Fig. 1a).

We found a mean value of  $k_{ep}$  in grade IV tumors of  $1.4\pm0.5 \text{ min}^{-1}$ , a mean value of  $k_{ep}$  in grade III tumors of  $1.2\pm0.5 \text{ min}^{-1}$ , and a mean value of  $k_{ep}$  in low-grade tumors of  $0.8\pm0.3 \text{ min}^{-1}$ . The mean values for  $r$  were  $0.057\pm0.095$ ,  $0.108\pm0.052$ , and  $0.086\pm0.051 \text{ min}^{-1}$  for grade IV, grade III, and low-grade tumors, respectively. A significant correlation for  $k_{ep}$  and  $r$  was found in all 75 ROIs ( $r=-0.63$ ,  $p<0.0001$ ; Fig. 1b).

The mean values for  $v_e$  were found to be  $0.18\pm0.10$  for grade IV tumors,  $0.14\pm0.05$  for grade III tumors, and  $0.04\pm0.03$  for low-grade tumors, while the mean values for  $\beta$  were instead found to be  $-12.9\pm9.1 \text{ min}^{-1}$  for grade IV tumors,  $-12.5\pm7.2 \text{ min}^{-1}$  for grade III tumors, and  $-4.7\pm1.3 \text{ min}^{-1}$  for low-grade tumors.

Figure 2 shows the distributions for  $K^{trans}$  and  $k_{ep}$  calculated by the ETK model and for  $a_0$  and  $r$  calculated by the EU1 algorithm for both high- (grade IV and III) and low-grade

tumors. Both theoretical models show adequate differentiation between low- and high-grade tumors, even if the ETK parameters seem to differentiate better than PUN indices. For low-grade tumors, the EU1 model shows low values of  $a_0$  (about  $a_0<25 \text{ min}^{-1}$ ) and  $r$  values that are almost all positive. However, the differentiation between grade IV and III is not adequate for both models. From this graph, it appears that the best parameters, in terms of usefulness for discriminating between low- and high-grade tumors, are  $K^{trans}$  for the DCE-MRI technique and  $a_0$  for the EU1 algorithm.

The quality of fitting of results between the two methods was assessed by standard  $R^2$  criterion: for the ETK model, we obtained a mean  $R^2=0.81$  (SD=0.09) for high-grade tumors and a mean  $R^2=0.82$  (SD=0.13) for low-grade tumors. For the EU1 class, we obtained a mean  $R^2=0.91$  (SD=0.06) for high-grade tumors and a mean  $R^2=0.85$  (SD=0.11) for low-grade tumors. The total mean  $R^2$  values (for high- and low-grade tumors) were 0.81 for the ETK model and 0.89 for the EU1 class, respectively. According to these  $R^2$  values, these two models appear to be equivalent.

In Fig. 3, we present an example of fitting by using the ETK model and the EU1 class, with their respective  $R^2$  values, in a patient with glioblastoma multiforme (WHO grade IV). The sensitivity and specificity of separating low- vs. high-grade tumors for  $K^{trans}$  were 98.0 and 92.0 %, respectively. The sensitivity and specificity for  $a_0$  were 89.0 and 92.0 %, respectively.

### Discussion

In recent years, DCE-MRI has been used to study tumors in the human body in order to differentiate between high- and low-grade tumors [27–29]. Different methods have been

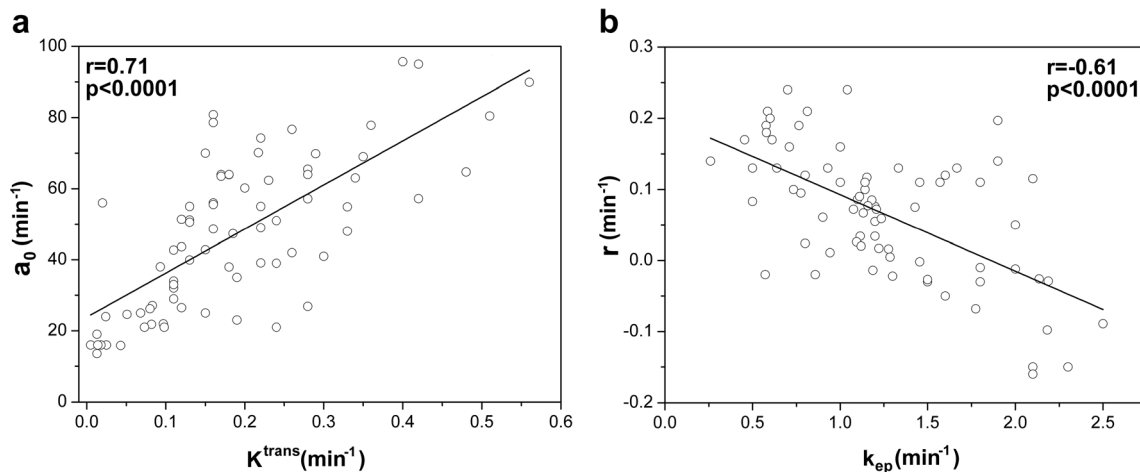


**Fig. 1** Pearson correlations and their respective correlation coefficient,  $r$  for different parameters: correlation between **a**  $K^{trans}$  and  $a_0$  and **b**  $k_{ep}$  and  $r$ . The range of  $r$  is between +1 and -1. A value of 0 indicates that there is

no association between the two variables. A value greater than 0 indicates a positive association, while a value lower than 0 indicates a negative association between the variables

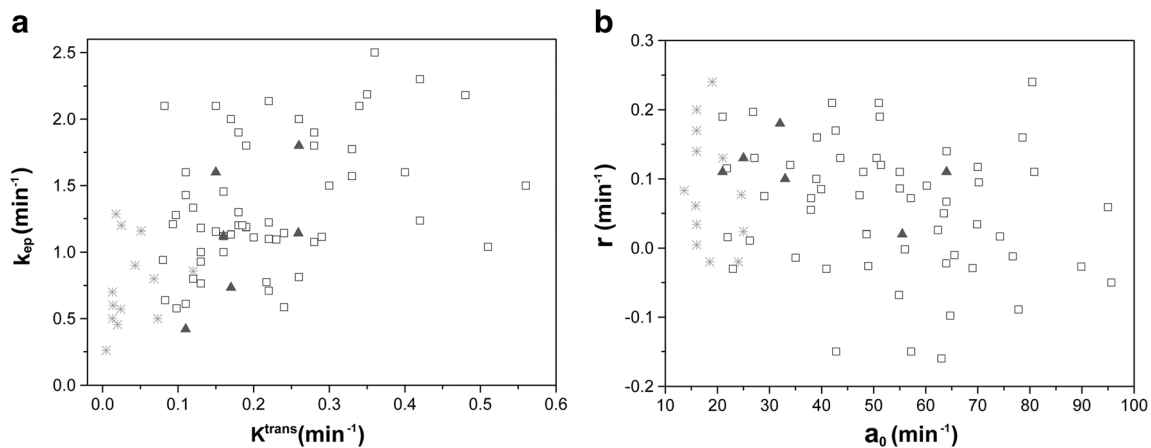


**Fig. 2** Feature distribution in the parametric planes for **a** the extended Tofts-Kety model ( $K^{\text{trans}}$  and  $k_{\text{ep}}$ ) and for **b** the EU1 class ( $a_0$  and  $r$ ). This figure shows grade IV tumors (squares), grade III tumors (triangles), and low-grade tumors (asterisks)

applied to analyze DCE-MRI experimental data [14]. By using these models, it is possible to obtain different kinetic parameters, such as  $K^{\text{trans}}$ ,  $k_{\text{ep}}$ ,  $v_p$ , and  $v_e$ .

The robustness and reproducibility of quantitative DCE-MRI studies rely on appropriately measuring AIF; in fact, errors in AIF estimation can seriously affect estimates of permeability parameters. Different approaches can be used to assess AIF. It is possible to use standard AIFs [30] or obtain them by individual measurements using different theoretical models, including mono-exponential [31] or bi-exponential [32] functions. The estimation of high-quality AIF is, however, difficult because of factors such as patient motion, partial volume effects, flow artifacts, limited temporal resolution, and difficulties in quantifying the peak concentrations of CA.

Another key point in the DCE-MRI studies is the evaluation of pre-contrast tissue  $T_1$  values, which can be achieved in

different ways. A pre-contrast  $T_1$  mapping is essential for converting dynamic image signal intensity into CA concentration in tissue and plasma to accurately evaluate permeability parameters.

On the other hand, phenomenological universalities (PUN) represent a novel tool for experimental research. This approach was originally developed by Delsanto et al. in 2007 [19], and has been used subsequently in different fields, including physics, engineering, social sciences, and medicine [21, 33]. The EU1 class, derived from the extended PUN description, is able to reproduce contrast uptake and wash-out phase giving high  $R^2$  values in the DCE-MRI experimental data fitting. Gliozzi et al. in 2011 [16] compared this class, the Weibull function [34] and the bi-exponential function in a small group of patients with spine tumors, finding that the EU1 results were very promising, obtaining high  $R^2$  values

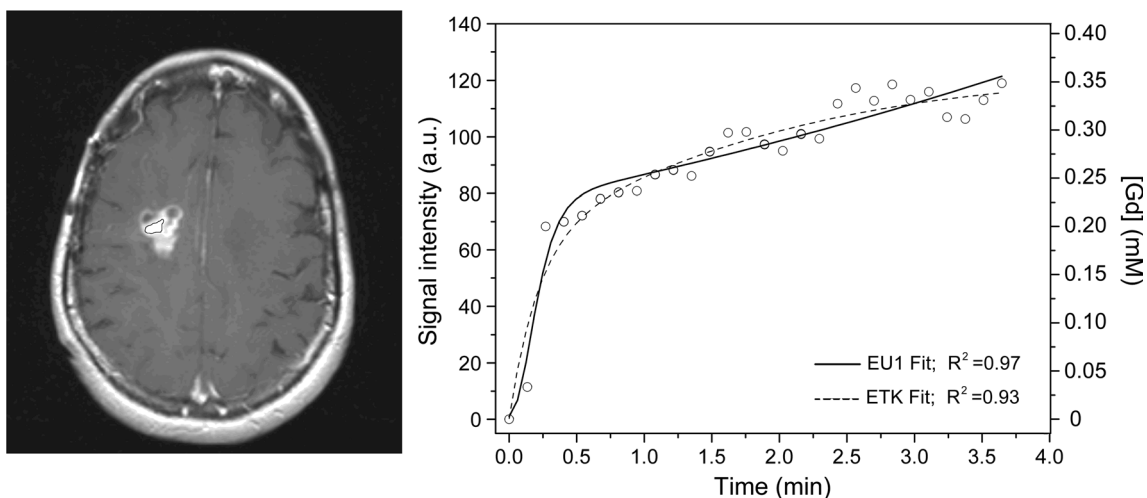


**Fig. 3** An example of fitting of DCE-MRI experimental data by using the extended Tofts-Kety model and the EU1 class, with their  $R^2$  values, respectively, in a 46-year-old female patient with glioblastoma multiforme (WHO grade IV). Empty circles represent experimental

data, continuous and dash lines are best fits obtained by Eq. (2) for ETK model, dash line) and Eq. (6) for EU1 class, continuous line). For this example, the  $R^2$  value is better in the EU1 class than in the ETK model

in the DCE-MRI data fitting. Subsequently, Mazzetti et al. in 2012 [17] compared the EU1 class and the ETK model in 28 patients with prostate tumors.

After reviewing Mazzetti et al.'s work, we decided to compare the ETK model and the EU1 algorithm in 30 adult patients with astrocytic tumors. We decided to employ this algorithm because there have been no studies that used the EU1 algorithm to study the brain tumors. Most importantly, we also chose to use these two functions because they are characterized by the same number of fitting parameters (namely, three). We analyzed 56 ROIs in grade IV tumors, six ROIs in grade III tumors, and 13 ROIs in low-grade tumors. Pearson correlations were assessed for different kinetic parameters. In our study, we utilized a ROI-based analysis that has the advantages of speed and ease of use.

Significant linear correlations were found when we compared the main fitting parameters obtained by the two models. The Pearson coefficient produced a significant correlation between  $K^{\text{trans}}$  and  $a_0$  for all 75 ROIs. A similar correlation was found between  $k_{\text{ep}}$  and  $r$  ( $p < 0.0001$ ).  $K^{\text{trans}}$  and  $a_0$  are related to the steepness of the DCE-MRI during the wash-in phase, while  $k_{\text{ep}}$  and  $r$  determine the behavior in the wash-out phase of the DCE-MRI curve.

The differentiation between high- and low-grade tumors is shown in Fig. 2, where it is possible to see that lower values of  $K^{\text{trans}}$  and  $a_0$  are related to low-grade tumors. Therefore, our results show that, in general, both  $K^{\text{trans}}$  and  $a_0$  are useful for differentiating high- from low-grade tumors. However, these parameters are not useful for differentiating between grades IV and III. In addition, we calculated the quality of data fitting by  $R^2$ , obtaining higher  $R^2$  values in the EU1 class than in the ETK model.

The limitations of this study were the low number of patients with low-grade and grade III tumors, and the fact that there was no assessment made of repeatability/reproducibility. Probably, the differentiation between low- and high-grade tumors would be more difficult should more grade III gliomas be included in the study. Moreover, due to patients' health conditions, we were not able to follow the CA contrast for a long time; therefore, the  $v_e$  values may not be accurate in all patients. In this study, we also did not explore the use of denoising in the DCE-MRI fitting. There are several algorithms that allow attenuation of denoising in data of this type. For instance, Gal et al. [34] presented the DNLM algorithm that permits a good attenuation of noise in the DCE-MRI analysis.

## Conclusions

In conclusion, the results showed that both models are equally capable of differentiating high- from low-grade gliomas with a relatively good correlation; hence, we can confirm that the

application of an empirical model to the DCE-MRI experimental data, in this case, the EU1 class, could be a useful alternative to pharmacokinetic models. The main limitation of the EU1 class is that it only allows us to estimate the permeability parameters from DCE-MRI data, thus giving partial information with respect to the ETK model, which also allows us to quantify tumor blood volume with the derived parameter  $v_p$ . Conversely, its strength is that, using this algorithm, the data analysis is more easily performed than with the ETK model, because it does not need an AIF assessment and a pre-contrast T1 map calculation. Moreover, since the EU1 class works on DCE-MRI signal intensity, its analysis is faster than with the ETK algorithm. Even if our results are not generalizable, our preliminary data suggest that the EU1 class can be used to assess tumor grade in astrocytic tumors as well as a pharmacokinetic model. In the future, the EU1 class could be utilized to define threshold values to differentiate high- from low-grade tumors.

**Acknowledgment** We thank Dr. Simone Mazzetti (Institute for Cancer Research and Treatment, Candiolo (TO), Italy) for his valuable help with the EU1 algorithm.

**Conflicts of Interest** The authors declare that they have no conflicts of interest concerning this article.

## References

- Gaitan MI, Shea CD, Evangelou IE, Stone RD, Fenton KM, Bielekova B, Massacesi L, Reich DS: Evolution of the blood–brain barrier in newly forming multiple sclerosis lesions. *Ann Neurol* 70: 22–29, 2011
- Lund H, Krakauer M, Skimminge A, Sellebjerg F, Garde E, Siebner HR, Paulson OB, Hesse D, Hanson LG: Blood–brain barrier permeability of normal appearing white matter in relapsing-remitting multiple sclerosis. *PLoS One* 8:e56375, 2013
- Taheri S, Gasparovic C, Huisa BN, Adair JC, Edmonds E, Prestopnik J, Grossetete M, Shah NJ, Wills J, Qualls C, Rosenberg GA: Blood–brain barrier permeability abnormalities in vascular cognitive impairment. *Stroke* 42:2158–2163, 2011
- Kassner A, Mandell DM, Mikulis DJ: Measuring permeability in acute ischemic stroke. *Neuroimaging Clin N Am* 21:315–325, 2011. x-xi
- Yuan F, Salehi HA, Boucher Y, Vasthare US, Tuma RF, Jain RK: Vascular permeability and microcirculation of gliomas and mammary carcinomas transplanted in rat and mouse cranial windows. *Cancer Res* 54:4564–4568, 1994
- Bullitt E, Zeng D, Gerig G, Aylward S, Joshi S, Smith JK, Lin W, Ewend MG: Vessel tortuosity and brain tumor malignancy: a blinded study. *Acad Radiol* 12:1232–1240, 2005
- Vick NA, Bigner DD: Microvascular abnormalities in virally induced canine brain tumors. Structural bases for altered blood–brain barrier function. *J Neurol Sci* 17:29–39, 1972
- Yankeelov TE, Gore JC: Dynamic contrast-enhanced magnetic resonance imaging in oncology: theory, data acquisition, analysis, and examples. *Curr Med Imaging Rev* 3:91–107, 2009
- Tofts PS, Brix G, Buckley DL, Evelhoch JL, Henderson E, Knopp MV, Larsson HB, Lee TY, Mayr NA, Parker GJ, Port RE, Taylor J,

- Weisskoff RM: Estimating kinetic parameters from dynamic contrast-enhanced T (1)-weighted MRI of a diffusable tracer: standardized quantities and symbols. *J Magn Reson Imaging* 10:223–232, 1999
10. Buckley DL: Uncertainty in the analysis of tracer kinetics using dynamic contrast-enhanced T1-weighted MRI. *Magn Reson Med* 47:601–606, 2002
  11. Padhani AR: Dynamic contrast-enhanced MRI in clinical oncology: current status and future directions. *J Magn Reson Imaging* 16:407–422, 2002
  12. Harrer JU, Parker GJ, Haroon HA, Buckley DL, Embelton K, Roberts C, Baleriaux D, Jackson A: Comparative study of methods for determining vascular permeability and blood volume in human gliomas. *J Magn Reson Imaging* 20:748–757, 2004
  13. Bergamino M, Saitta L, Barletta L, Bonzano L, Mancardi GL, Castellani L, Ravetti JL, Roccatagliata L: Measurement of blood–brain barrier permeability with T1-weighted dynamic contrast-enhanced MRI in brain tumors: a comparative study with two different algorithms. *ISRN Neuroscience* 2013:6 pages, 2013
  14. Bergamino M, Bonzano L, Levrero F, Mancardi GL, Roccatagliata L: A review of technical aspects of T-weighted dynamic contrast-enhanced magnetic resonance imaging (DCE-MRI) in human brain tumors. *Phys Med*, 2014
  15. Fan X, Medved M, Karczmar GS, Yang C, Foxley S, Arkani S, Recant W, Zamora MA, Abe H, Newstead GM: Diagnosis of suspicious breast lesions using an empirical mathematical model for dynamic contrast-enhanced MRI. *Magn Reson Imaging* 25:593–603, 2007
  16. Gliozzi AS, Mazzetti S, Delsanto PP, Regge D, Stasi M: Phenomenological universalities: a novel tool for the analysis of dynamic contrast enhancement in magnetic resonance imaging. *Phys Med Biol* 56:573–586, 2011
  17. Mazzetti S, Gliozzi AS, Bracco C, Russo F, Regge D, Stasi M: Comparison between PUN and Tofts models in the quantification of dynamic contrast-enhanced MR imaging. *Phys Med Biol* 57:8443–8453, 2012
  18. Castorina P, Delsanto PP, Guiot C: Classification scheme for phenomenological universalities in growth problems in physics and other sciences. *Phys Rev Lett* 96:188701, 2006
  19. Delsanto PP: Universality of nonclassical nonlinearity: applications to non-destructive evaluations and ultrasonics, New York, 2007
  20. Barberis L, Condat CA, Gliozzi AS, Delsanto PP: Concurrent growth of phenotypic features: a phenomenological universalities approach. *J Theor Biol* 264:123–129, 2010
  21. Delsanto PP, Gliozzi AS, Guiot C: Scaling, growth and cyclicity in biology: a new computational approach. *Theor Biol Med Model* 5:5, 2008
  22. Louis DN, Ohgaki H, Wiestler OD, Cavenee WK, Burger PC, Jouvet A, Scheithauer BW, Kleihues P: The 2007 WHO classification of tumours of the central nervous system. *Acta Neuropathol* 114:97–109, 2007
  23. Jenkinson M, Bannister P, Brady M, Smith S: Improved optimization for the robust and accurate linear registration and motion correction of brain images. *NeuroImage* 17:825–841, 2002
  24. Schabel MC: A unified impulse response model for DCE-MRI. *Magn Reson Med* 68:1632–1646, 2012
  25. Haase A: Snapshot FLASH MRI. Applications to T1, T2, and chemical-shift imaging. *Magn Reson Med* 13:77–89, 1990
  26. van Rijswijk CS, Geirnaert MJ, Hogendoorn PC, Taminiau AH, van Coevorden F, Zwinderman AH, Pope TL, Bloem JL: Soft-tissue tumors: value of static and dynamic gadopentetate dimeglumine-enhanced MR imaging in prediction of malignancy. *Radiology* 233:493–502, 2004
  27. Stoyanova R, Huang K, Sandler K, Cho H, Carlin S, Zanzonico PB, Koutcher JA, Ackerstaff E: Mapping tumor hypoxia in vivo using pattern recognition of dynamic contrast-enhanced MRI data. *Transl Oncol* 5:437–447, 2012
  28. Heller SL, Moy L, Lavianlivi S, Moccaldi M, Kim S: Differentiation of malignant and benign breast lesions using magnetization transfer imaging and dynamic contrast-enhanced MRI. *J Magn Reson Imaging* 37:138–145, 2013
  29. Franiel T, Hamm B, Hricak H: Dynamic contrast-enhanced magnetic resonance imaging and pharmacokinetic models in prostate cancer. *Eur Radiol* 21:616–626, 2011
  30. Tofts PS, Kermode AG: Measurement of the blood–brain barrier permeability and leakage space using dynamic MR imaging. 1. Fundamental concepts. *Magn Reson Med* 17:357–367, 1991
  31. Zhang N, Zhang L, Qiu B, Meng L, Wang X, Hou BL: Correlation of volume transfer coefficient  $K_{trans}$  with histopathologic grades of gliomas. *J Magn Reson Imaging* 36:355–363, 2012
  32. Eliat PA, Olivie D, Saikali S, Carsin B, Saint-Jalmes H, de Certaines JD: Can dynamic contrast-enhanced magnetic resonance imaging combined with texture analysis differentiate malignant glioneuronal tumors from other glioblastoma? *Neurol Res Int* 2012:195176, 2012
  33. Gliozzi AS, Guiot C, Delsanto PP: A new computational tool for the phenomenological analysis of multipassage tumor growth curves. *PLoS One* 4:e5358, 2009
  34. Gal Y, Mehnert A, Bradley A, McMahon K, Crozier S: An evaluation of four parametric models of contrast enhancement for dynamic magnetic resonance imaging of the breast. *Conf Proc IEEE Eng Med Biol Soc* 2007:71–74, 2007